CHEMISTRY OF MATERIALS

pubs.acs.org/cm

Article

Thermoelectric and Magnetic Behavior of $(Eu/Yb/Mg)_2Si$ Zintl Phases Grown in Magnesium-Based Flux

Published as part of Chemistry of Materials special issue "Honoring the Outstanding Contributions of Mercouri Kanatzidis to Chemistry of Materials".

Olufemi S. Araoyinbo, Amirhossein Zareihassangheshlaghi, Md Sahab Uddin, Mehak Ghafoor, Kaya Wei, and Susan E. Latturner*

Cite This: *Chem. Mater.* 2026, 38, 1875−1884

Read Online

ACCESS | Metrics & More | Article Recommendations | Supporting Information

ABSTRACT: Reactions of silicon with europium and ytterbium were carried out in Mg/Zn eutectic flux to synthesize complex metal silicides. Depending on the ratios of Eu and Yb reactant used, observed products were Yb_2MgSi_2 (when no Eu was used), $Eu_2Yb_{2.7}Mg_{9.3}Si_7$ (with more Yb than Eu reacted), and $Eu_5(Eu_{1-x}Yb_x)_3Mg_{16}Si_{12}$ (with more Eu than Yb). The latter two compounds form in the $Zr_2Fe_{12}P_7$ (*P*-6) and $Ho_5Ni_{19}P_{12}$ (*P*-62*m*) structure types, and are charge-balanced Zintl phases. Density of states calculations show that the consistently observed composition of $Eu_2Yb_{2.7}Mg_{9.3}Si_7$ is electronically stabilized. Magnetic susceptibility measurements show europium and ytterbium are both divalent; highly anisotropic ferromagnetic ordering of Eu^{2+} moments is observed at low temperature. Thermoelectric measurements indicate that site mixing of cations lowers thermal conductivity, and that $Eu_{6.72}Yb_{1.28}Mg_{15.56}Zn_{0.44}Si_{12}$ has the most promising thermoelectric behavior with a zT = 0.14 at 400 K and potential for use at high temperatures.

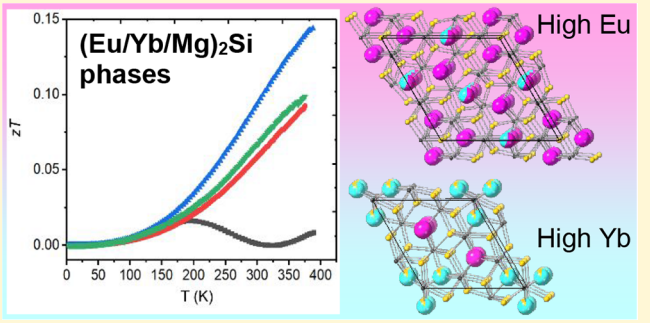

INTRODUCTION

Zintl phases are a broad class of intermetallic compounds comprised of very electropositive metals (groups 1 and 2, as well as some divalent rare earths) and main group metalloids.[1] The metalloids accept electrons from the metals to fill their valence shells, sometimes forming polyanions with covalent M−M bonds. This results in anions that are charge-balanced by surrounding metal cations, resulting in semiconducting or semimetallic behavior. Complex structures and incorporation of heavy elements lower the thermal conductivity, which makes them promising as thermoelectric materials, exemplified by $Yb_{14}MnSb_{11}$, SrAgSb, and $Sr_{7.8}Mg_{16.2}Si_{12}$.[2−4] The thermoelectric behavior of a material is quantified by its figure of merit ($zT = [S^2\sigma/\kappa]T$) which depends on Seebeck coefficient S, electrical conductivity σ, and thermal conductivity κ. Zintl phases containing heavy cations such as europium and ytterbium often exhibit lower thermal conductivity due to scattering of phonons, particularly if they exhibit disorder such as site mixing. Incorporation of europium as the electropositive metal can also induce magnetic ordering or magnetoresistive behavior, which was reported for EuMgSn and $EuIn_2P_2$.[5,6] Exploring the synthesis of Zintl phases and investigating the correlations between their structures and properties are therefore of interest in many research fields.

Zintl phases are often produced using the traditional solid-state synthesis method which uses high temperature heating of stoichiometric ratios to ensure sufficient diffusion of reactants to drive product formation.[7] This method favors the most thermodynamically stable product formation, and is less amenable for exploratory synthesis or isolation of metastable compounds. For exploratory synthesis of complex structures, reactions must be designed such that sufficient diffusion is achieved at lower temperature. In metal flux synthesis, the use of a low-melting metal as a solvent allows reactions to be carried out below the temperature of traditional solid-state methods.[8] Slow cooling of the homogeneous solution enables products to form as large crystals. Modifying the cooling rate may stabilize the formation of different products; two different Ba/Yb/Mg/Si compounds precipitate from Mg/Al melts depending on this factor.[9] The use of solution chemistry also introduces the possibility of precipitation of a high temperature

Received: November 3, 2025
Revised: January 26, 2026
Accepted: January 30, 2026
Published: February 7, 2026

product in the flux which may convert to a different compound as the temperature of the flux is lowered. This was recently reported for reactions of cerium with several different transition metals in molten gallium.[10]

Flux reactions are particularly attractive as a method to grow metal silicides; dissolution in a molten metal makes silicon reactive well below its melting point. Complex silicide compounds can be grown from gallium flux ($Ba_8Ga_{16}Si_{30}$, $SmNiSi_3$), aluminum flux ($U_{1.33}Ni_4Al_{48}Si$, $Gd_2AuAl_6Si_4$), and indium flux ($YbCo_xSi_{2-x}$, $Sc_2Mn_4Si_5$).[11−16] Magnesium metal is not typically thought of as a flux due to its high melting point and volatility, but combining it with a secondary flux component such as Zn can result in eutectic formation (Mg/Zn eutectic with 72:28 mol ratio melts at 341 °C), and the use of sealed Nb ampules prevents evaporation. In our previous work, we explored the reactions of electropositive divalent metals (A = Ca, Sr, Ba, Eu, Yb) with different tetrel elements (Tt = Si, Ge, Sn) in Mg/Al flux mixtures.[4,5,9,17,18] Nineteen compounds were reported which demonstrates the flexibility of flux synthesis. These compounds can be represented with a general formula $(A/Mg)_2Tt$, and are thus charge balanced. They all are semimetallic and exhibit complex hexagonal structures ($Ho_{20}Ni_{66}P_{43}$, $Ho_5Ni_{19}P_{12}$, $Ho_6Ni_{20}P_{13}$, and $Zr_2Fe_{12}P_7$-type). They also have potential magnetic and thermoelectric applications.

In this work, we explored reactions of silicon with varying ratios of europium and ytterbium, using Mg/Zn as a flux. The $(Eu/Yb/Mg)_2Si$ products were found to exhibit two structure types depending on the Eu:Yb ratio. Magnetic susceptibility data indicates europium and ytterbium are both divalent in these materials, with ferromagnetic ordering of Eu^{2+} moments observed in all compounds. Eu/Yb site mixing is observed to lower thermal conductivity, and particularly promising thermoelectric behavior is seen for $Eu_{6.72}Yb_{1.28}Mg_{15.56}Zn_{0.44}Si_{12}$.

EXPERIMENTAL PROCEDURE

Synthesis

To carry out flux reactions, desired stoichiometric ratios of europium (99%, Alfa Aesar) and ytterbium chunks (99.9%, Alfa Aesar) were weighed and loaded into a niobium tube containing 22 mmol of magnesium slugs (99.95% Alfa Aesar), 8 mmol of zinc shot (99.99%, Alfa Aesar) and 3 mmol silicon powder (99.9%, Beantown Chemical) in an argon-filled glovebox. The reaction ratios are listed in Table 1.

Table 1. Amounts (In Millimoles) of Europium and Ytterbium Reacted with 3 mmol of Si in a 22:8 mmol Mg/Zn Flux and the Resulting Product Compositions Determined from X-ray Refinement and Elemental Analysis

Eu/Yb (mmoles)	Refined composition (SC-XRD)	Elemental Analysis (SEM-EDS)[a]	Structure type
0:3	Yb_2MgSi_2	$Yb_{1.8}Mg_{1.0}Si_{2.1}$	Mo_2FeB_2
0.5:2.5	$Eu_2Yb2.69(1)Mg_{9.31}Si_7$	$Eu_{2.0}Yb_{2.8}Mg_{9.8}Si_7$	$Zr_2Fe_{12}P_7$
1.0:2.0	$Eu_2Yb2.69(1)Mg_{9.31}Si_7$	$Eu_{2.1}Yb_{2.6}Mg_{9.5}Si_7$	$Zr_2Fe_{12}P_7$
1.5:1.5	$Eu_2Yb2.65(1)Mg_{9.35}Si_7$	$Eu_{2.3}Yb_{2.6}Mg_{9.6}Si_7$	$Zr_2Fe_{12}P_7$
2.0:1.0	$Eu_{6.50}Yb1.50(2)$ $Mg_{15.56}Zn0.44(2)$ Si_{12}	$Eu_{6.1}Yb_{2.3}Mg_{17.2}Si_{12}$	$Hf_2Co_4P_3$
2.25:0.75	$Eu_{6.72}Yb1.28(2)$ $Mg_{15.56}Zn0.44(2)Si_{12}$	$Eu_{6.5}Yb_{2.0}Mg_{16.9}Si_{12}$	$Hf_2Co_4P_3$
2.5:0.5	$Eu_{7.46}Yb0.54(1)$ $Mg_{15.56}Zn0.44(1)Si_{12}$	$Eu_{7.3}Yb_{1.0}Mg_{15.9}Si_{12}$	$Hf_2Co_4P_3$
3:0	$Eu_8Mg_{15.71}Zn0.29(1)Si_{12}$	$Eu_{7.8}Mg_{18}Si_{12}$	$Hf_2Co_4P_3$

[a]Error values for SEM-EDS compositions are 5%.

The niobium crucible was welded in an argon-filled glovebox and then flame-sealed into quartz tubes under vacuum. All reaction ampules were placed in a furnace and heated from room temperature to 1273 K in 5 h, held at 1273 K for 10 h, cooled to 1023 K in 80 h, and held at 1023 K for 24 h, at which point the reaction ampules were quickly removed from the furnace, inverted and centrifuged to remove excess flux. *(Caution: use suitable protective equipment including gloves, tongs, and face shield to transfer the hot ampule.)* During this process, crystals adhere to the sides at one end of the niobium crucible as the flux is decanted. The crucibles were then cut open and crystals of product were removed.

Elemental Analysis

SEM-EDS analyses were carried out using a FEI Nova 400 NanoSEM equipped with energy dispersive spectroscopy (EDS) capabilities. The samples were mounted on aluminum pucks using carbon tape. The samples were analyzed using an acceleration voltage of 25 kV. Some regions of the crystal surfaces retained remnants of flux droplets (Figure S1, Supporting Information), necessitating measurements to be conducted on either cleaved samples or areas free from flux. The resulting data on cleaved samples do not show the presence of any zinc from the flux or elemental incorporation from the niobium crucible used in the process. The observed compositions are listed in Table 1.

Structural Characterization

Products were examined under an optical microscope and tiny crystals with shiny surfaces were mounted on Hampton Cryoloop holders using Parabar oil. Single-crystal X-ray diffraction (SCXRD) data were collected using a Rigaku XtaLAB Synergy-S diffractometer equipped with a Mo−Kα (λ = 0.7107 Å) source. Data were collected at room temperature, and the structure solution was determined by direct methods and refined using SHELXTL program suite.[19] Yb_2MgSi_2 exhibited the Mo_2FeB_2 structure type in the tetragonal space group *P4/mbm*. The structures of the $Eu_2Yb_xMg_{12-x}Si_7$ compounds were refined in the $Zr_2Fe_{12}P_7$ structure type in hexagonal space group *P-6*. $Eu_5(Eu_{1-x}Yb_x)_3Mg_{16}Si_{12}$ compounds formed in the $Hf_2Co_4P_3$ structure type in hexagonal space group *P-62m*. The high symmetry *1a* Wyckoff position in the $Hf_2Co_4P_3$-type structures (occupied by Mg) exhibited negative thermal parameters. Face indexing of the crystals and associated numerical absorption corrections were ineffective at resolving this. Upon allowing occupancy refinement, this site refined to greater than unity with a significant lowering of the R-value. Given the short distances to neighboring atoms, it is unlikely that Yb^{2+} or Eu^{2+} are mixing on this site. While the presence of zinc was not seen in elemental analysis, it is possible that trace amounts mix on this site, given the very similar sizes of Mg^{2+} and Zn^{2+}. This site was therefore refined as a Mg/Zn mixed site (leading to 30−44% Zn occupancy) which yielded a lower R-value with no negative thermal parameters. Crystallographic information for these compounds is shown in Table 2 and Supporting Information Table S1; Crystallographic Information Files are available from the CCDC under deposition numbers listed in the tables.

Powder X-ray Diffraction

Samples isolated from the flux reactions were ground to powder in an alumina mortar and pestle. The powders were placed on a zero-background sample holder and diffraction data were acquired using a Rigaku SmartLab diffractometer with a Cu−Kα radiation source. Data were collected in the 2θ range 10°−80°. The resulting patterns were analyzed with the search-match feature and compared to calculated powder patterns to determine the products present in the sample. Rietveld refinement of the data of mixed phase product was performed using the GSAS-II software package.[20]

Calculations of Electronic Structure

The possible electronic stabilization of $Eu_2Yb_{2.65}Mg_{9.35}Si_7$ (a product composition consistently observed for this structure type) was investigated via density of states (DOS) calculations employing the Stuttgart TB-LMTO-ASA software. These computations made use of the atomic coordinates obtained from single-crystal X-ray diffraction

https://doi.org/10.1021/acs.chemmater.5c02941
Chem. Mater. 2026, 38, 1875−1884

Table 2. Crystallographic Data and Collection Parameters for Four Representative (Eu/Yb/Mg/Si) Phases; the Remainder Are Found in Supporting Information (Table S1)

Compound	Yb_2MgSi_2	$Eu_2Yb_{2.65}Mg_{9.35}Si_7$	$Eu_{6.50}Yb_{1.50}Mg_{15.56}Zn_{0.44}Si_{12}$	$Eu_{7.46}Yb_{0.54}Mg_{15.56}Zn_{0.44}Si_{12}$
F.W. (g/mol)	426.61	1186.46	1991.41	1971.17
Crystal system	Tetragonal	Hexagonal	Hexagonal	Hexagonal
Space group	*P4/mbm*	*P-6*	*P-62m*	*P-62m*
Temperature (K)	297(2)	297(2)	297(2)	297(2)
radiation	Mo Kα	Mo Kα	Mo Kα	Mo Kα
a (Å)	7.0526 (2)	11.1217(2)	14.6242(2)	14.6421(2)
c (Å)	4.1327 (2)	4.3886(1)	4.3968(1)	4.4069(1)
Z	2	1	1	1
V(Å)	205.563 (2)	470.11(2)	814.35(3)	818.22(3)
Dx(g/cm^3)	6.892	4.191	4.061	4.000
Limiting indices	$-11 < h < 11$	$-18 < h < 18$	$-22 < h < 23$	$-23 < h < 23$
	$-11 < k < 11$	$-18 < k < 17$	$-23 < k < 24$	$-23 < k < 23$
	$-6 < l < 6$	$-7 < l < 7$	$-7 < l < 7$	$-7 < l < 7$
No. of reflections	287	1552	1445	1450
No. of parameters	12	45	46	46
μ (mm−1)	45.715	20.363	17.636	16.649
GOF	1.183	1.077	1.063	1.065
R1/wR2 (all data)	0.0167/0.0337	0.0191/0.0364	0.0158/0.0291	0.0205/0.0468
R1/wR2 (I > 2σ(I))	0.0140/0.0306	0.0186/0.0362	0.0154/0.0289	0.0199/0.0465
highest peak/hole (e−/A^3)	1.595/-1.931	1.085/-1.694	1.106/-0.867	4.913/-1.179
CCDC deposition	2498789	2498651	2498703	2498706

analyses.[21,22] Due to the computational difficulties imparted by partially filled f-shells, we substituted Sr for Eu and Ca for Yb. To minimize the computing challenges of Yb/Mg site mixing, we considered two ordered models, with the mixed site occupied either by Mg or Yb. The resulting compounds ($Eu_2Mg_{12}Si_7$ and $Eu_2Yb_3Mg_9Si_7$) are modeled as $Sr_2Mg_{12}Si_7$ and $Sr_2Ca_3Mg_9Si_7$.

Magnetic Susceptibility Measurements

Magnetic susceptibility data were collected on single crystals using a Quantum Design MPMS SQUID magnetometer to explore potential magnetic ordering and to determine the valence state of europium and ytterbium. Rod-shaped crystals of $Eu_2Yb_{2.65}Mg_{9.35}Si_7$, $Eu_{6.50}Yb_{1.50}Mg_{15.56}Zn_{0.44}Si_{12}$, $Eu_{6.72}Yb_{1.28}Mg_{15.56}Zn_{0.44}Si_{12}$, $Eu_{7.46}Yb_{0.54}Mg_{15.56}Zn_{0.44}Si_{12}$ and $Eu_8Mg_{15.71}Zn_{0.29}Si_{12}$ were positioned with their crystallographic *c*-axis either perpendicular or parallel to the applied field by aligning it on a Kapton tape. Following that, this tape was put into a straw and fastened to the sample rod of the magnetometer. Magnetic susceptibility, expressed as χ = M/H, was measured from 1.8 to 300 K with a 500 Oe applied magnetic field. Zero-field-cooled (ZFC) and field-cooled (FC) data were also collected with the *c*-axis of the crystals parallel and perpendicular to the magnetic field from 1.8 to 300 K with a 500 Oe applied magnetic field. Measurements of magnetization were collected at 2 K as the field scaled from 7.0 to −7.0 T for both orientations of the crystals.

Thermoelectric Measurements

Single crystals of $Eu_2Yb_{2.65}Mg_{9.35}Si_7$, $Eu_{6.50}Yb_{1.50}Mg_{15.56}Zn_{0.44}Si_{12}$, $Eu_{6.72}Yb_{1.28}Mg_{15.56}Zn_{0.44}Si_{12}$, and $Eu_8Mg_{15.71}Zn_{0.29}Si_{12}$ were affixed onto a specially designed holder with silver epoxy. The electric current and the heat gradient were aligned with the long axis of the crystals (crystallographic *c*-axis). Thermal conductivity and Seebeck coefficients for the samples were determined using the classic one-heater-two-thermometer technique. We utilized two Cernox sensors as thermometers and a refined, polished metallic chip as the heating element. Incremental power was supplied to the heater, inducing stepwise thermal gradients through the specimens. The resulting temperature differences and thermoelectric voltages were recorded concurrently once the system reached thermal equilibrium at each power increment. Separately, electrical resistivity was measured on the same crystals using a four-wire configuration within a Quantum Design Physical Property Measurement System (PPMS) in the temperature range from 1.8 to 400 K.

RESULTS AND DISCUSSION

Synthesis

The Zintl phases $Eu_2Yb_{2.65}Mg_{9.35}Si_7$ and $Eu_5(Eu_{1-x}Yb_x)_3Mg_{16}Si_{12}$ ($0 < x < 0.5$) can be grown as large crystals from the reaction of silicon with europium and ytterbium in excess magnesium−zinc flux. Examples of single crystals grown are shown in Figure 1, which grow as silver rods

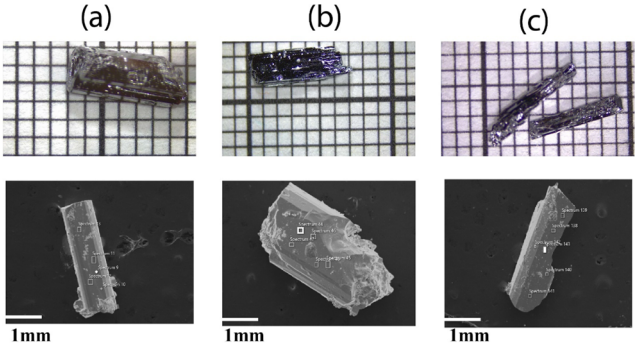

Figure 1. Optical microscopy images (top, on mm grid paper) and SEM images (bottom) of (a) $Eu_2Yb_{2.65}Mg_{9.35}Si_7$, (b) $Eu_{6.50}Yb_{1.50}Mg_{15.56}Zn_{0.44}Si_{12}$, and (c) $Eu_{6.72}Yb_{1.28}Mg_{15.56}Zn_{0.44}Si_{12}$.

up to 7 mm in length and 3 mm in diameter. Droplets of flux residues are seen on the surface of single crystals analyzed by SEM-EDX. These crystals are air stable and show no sign of oxidation after exposure to air for weeks. They dissolve readily in 1 M HCl.

In the absence of europium, crystals of Yb_2MgSi_2 are formed with the Mo_2FeB_2 structure type; this compound was previously reported by Nesper.[23] However, the introduction of europium at low concentrations (Eu amounts between 0.5 and 1.5 mmol) results in the formation of $Eu_2Yb_{2.65}Mg_{9.35}Si_7$ with the $Zr_2Fe_{12}P_7$ structure type. The PXRD data (Figure 2) show a mixture of Yb_2MgSi_2 and $Eu_2Yb_{2.65}Mg_{9.35}Si_7$ is present

https://doi.org/10.1021/acs.chemmater.5c02941
Chem. Mater. 2026, 38, 1875−1884

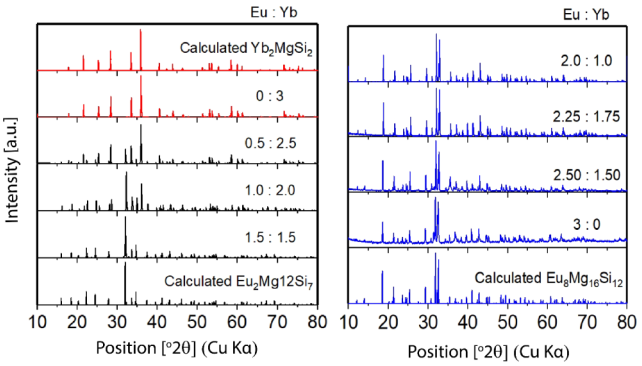

Figure 2. PXRD data for products formed at different Eu:Yb ratios reacting with silicon in Mg/Zn flux, compared with calculated patterns for Yb_2MgSi_2 (red), $Eu_2Mg_{12}Si_7$ (black), and $Eu_8Mg_{16}Si_{12}$ (blue).

at Eu/Yb reactant ratios up to 1.0:2.0 mmol. Rietveld refinement of the PXRD data for the product of the Eu/Yb 0.5:2.5 mmol ratio indicates 26% Yb_2MgSi_2 and 74% $Eu_2Yb_{2.65}Mg_{9.35}Si_7$ (Figure S2, Supporting Information). With a Eu reactant amount of 1.50 mmol, the product consists of pure $Eu_2Yb_{2.65}Mg_{9.35}Si_7$. The atomic percentages indicated by EDX are consistent with the stoichiometry obtained through single crystal X-ray diffraction (SC-XRD) refinement. As the europium content increases further (2 mmol of Eu and higher), the reaction abruptly switches to formation of $Hf_2Co_4P_3$-type compounds, with no byproducts seen in the PXRD data. The $Eu_5(Eu_{1-x}Yb_x)_3Mg_{16}Si_{12}$ products exhibit solid solution behavior, with increasing Eu content on a mixed site as the [Eu] is increased in the flux. In the absence of ytterbium, crystals of $Eu_8Mg_{16}Si_{12}$ are produced. However, a few such reactions yield crystals of TiNiSi-type EuMgSi, possibly resulting from insufficient mixing of reactants in those cases.

A magnesium-rich flux medium appears necessary to isolate many of the compounds described in this work. A stoichiometric reaction targeting $Eu_8Mg_{16}Si_{12}$ (1 mmol Eu, 2 mmol Mg, and 1.5 mmol Si heated to 1273 K, then cooled to room temperature in 12 h) yielded EuMgSi with the TiNiSi structure type, as well as some crystals of Mg_2Si. The PXRD data are found in Supporting Information (Figure S3). Carrying out the same reaction with added Mg/Zn flux produced $Eu_8Mg_{16}Si_{12}$. $(A/Mg)_2Si$ Zintl phases can be grown in either Mg/Zn or Mg/Al fluxes. Our previous work using Mg/Al flux mixtures yielded products that consistently contain up to 3−5% of aluminum, indicated by SEM-EDS measurements. However, determining where the Al is incorporated was not possible; it will either mix on a Mg site or Si site and SC-XRD is not able to distinguish this due to similar electron counts. On the other hand, SEM-EDS analysis of products grown in Mg/Zn flux did not detect any zinc. It was only upon allowing SC-XRD occupancy refinement that one Mg site in the $Hf_2Co_4P_3$-type compounds ($Eu_5(Eu_{1-x}Yb_x)_3Mg_{16}Si_{12}$) consistently indicated a mixing with a heavier element of similar size. The resulting refined compositions (for instance, $Eu_{6.72}Yb_{1.28}Mg_{15.56}Zn_{0.44}Si_{12}$) have 1.2% Zn, which is below the detection limit of our SEM-EDS. So it is likely that both possible fluxes (Mg/Zn and Mg/Al) allow the non-Mg flux component to incorporate into products, but Zn goes in at lower amounts.

Structures

The (Mg/Zn)/Si/Yb reaction produced Yb_2MgSi_2 with the tetragonal Mo_2FeB_2 structure type; this is shown in Figure 3.

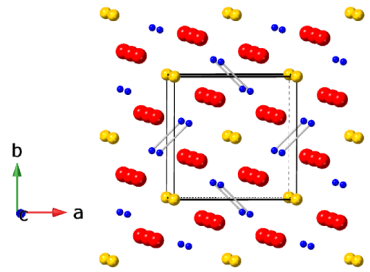

Figure 3. Structure of Yb_2MgSi_2 featuring Si−Si dimers. Mg sites are represented by yellow spheres, Yb sites are represented by red spheres, and Si sites are represented by blue spheres.

The notable structural feature is the Si−Si dimer with a bond length of 2.387(3) Å. This can be viewed as $[Si-Si]^{6-}$, which is charge-balanced by divalent ytterbium and magnesium, resulting in the Zintl phase formula $(Yb^{2+})_2(Mg^{2+})([Si_2]^{6-})$. Reactions with only europium yield the other endmember $Eu_8Mg_{15.71}Zn_{0.29}Si_{12}$. The composition has 24 divalent cations (Eu^{2+}, Zn^{2+}, and Mg^{2+}) charged-balanced by 12 Si^{4-} anions. This compound can be viewed as having either the $Hf_2Co_4P_3$ or $Ho_5Ni_{19}P_{12}$ structure type. These are isopointal hexagonal (P-62*m*) structures, which becomes apparent when the composition of the former is quadrupled ($Hf_8Co_{16}P_{12}$ versus $Ho_5Ni_{19}P_{12}$). Both have three unique phosphide sites and two large metal atom sites (2*c* and 3*g* Wyckoff sites). The difference occurs in the occupancy of a 3*f* site. In "$Hf_8Co_{16}P_{12}$", the 3*f* site is occupied by the large metal atom Hf. In $Ho_5Ni_{19}P_{12}$, it is occupied by a smaller transition metal Ni. Our ongoing survey of flux growth of $A_{5+x}Mg_{19-x}Si_{12}$ phases (A = Sr, Ba, Eu) results in compounds that may have this 3*f* site occupied by Mg ($Ba_5Mg_{19}Si_{12}$, isostructural to $Ho_5Ni_{19}Si_{12}$), by the larger A cations ($Eu_8Mg_{16}Si_{12}$), or by a mixture of Mg and A ($Sr_{7.8}Mg_{16.2}Si_{12}$).[4] Given this range of possible occupancies of this site, we typically use the $Ho_5Ni_{19}Si_{12}$ formulation. However, given that $Eu_8Mg_{15.71}Zn_{0.29}Si_{12}$ has europium fully occupying the 2*c*, 3*g*, and 3*f* sites, it is also accurate to assign this to the $Hf_2Co_4P_3$ structure type and refer to it as $Eu_2Mg_4Si_3$. This was the composition given by Numakura et al. in a recent report.[24]

In $Eu_8Mg_{15.71}Zn_{0.29}Si_{12}$, the bond length between europium in the 3*f* site and silicon falls within 3.007(5) Å and 3.173(2) Å (see Table 3). This is on the lower end of reported Eu−Si bond lengths, compared to those seen in $EuSi_2$ (3.12−3.24 Å) and Eu_5Si_3 (3.17−3.27 Å).[25,26] It is also significantly shorter than the distances between silicon and europium occupying the 3*g* and 2*c* Wyckoff sites (3.400−3.435 Å). This is because the 3*f* site is often occupied by smaller cations (and/or magnesium) while the bigger cations occupy the 3*g* and 2*c* sites. The above signals the difference between the $Hf_2Co_4P_3$ and $Ho_5Ni_{19}P_{12}$ structure types, where the bigger cation (Ho) occupies the 2*c* and 3*g* sites and the smaller cation (Ni) occupies the 3*f* site.

The presence of both ytterbium and europium in the reaction introduces formation of multiple phases and compounds with cation mixing. Reactions with high Yb content yield Yb_2MgSi_2 and/or $Eu_2Yb_{2.65}Mg_{9.35}Si_7$, with the ratio of these products dependent on the Eu:Yb ratio. The

https://doi.org/10.1021/acs.chemmater.5c02941
Chem. Mater. 2026, 38, 1875−1884

Table 3. Comparison of the Mixed Site Occupancy and Bond Lengths of the $Eu_5(Eu/Yb)_3Mg_{16}Si_{12}$ Products

	$Eu_{6.50}Yb_{1.50}Mg_{15.56}Zn_{0.44}Si_{12}$	$Eu_{6.72}Yb_{1.28}Mg_{15.56}Zn_{0.44}Si_{12}$	$Eu_{7.46}Yb_{0.54}Mg_{15.56}Zn_{0.44}Si_{12}$	$Eu_8Mg_{15.71}Zn_{0.29}Si_{12}$
Unit cell parameters	a = 14.6242 (2) Å	a = 14.6400 (2) Å	a = 14.6421 (2) Å	a = 14.7096 (2) Å
	c = 4.3968 (1) Å	c = 4.4029 (1) Å	c = 4.4069 (1) Å	c = 4.4303 (1) Å
2c site occupancy	Eu (100%)	Eu (100%)	Eu (100%)	Eu (100%)
3g site occupancy	Eu (100%)	Eu (100%)	Eu (100%)	Eu (100%)
3f site occupancy	44.0 (3) %Eu	50.0 (3) %Eu	76.0 (4) % Eu	100.0%Eu
	56.0 (3) %Yb	50.0 (3) %Yb	24.0 (4) %Yb	
3f site—Si	2.953 (3) Å	2.960 (3) Å	2.970(4) Å	3.007 (3) Å
	3.1391 (3) Å × 4	3.1453(4) Å × 4	3.1522 (3) Å × 4	3.1751 (3) Å × 4
3f site—Mg	3.225 (3) Å × 2	3.226 (3) Å × 2	3.230 (4) Å × 2	3.244 (3) Å × 2
	3.243 (3) Å × 2	3.246 (3) Å × 2	3.246 (4) Å × 2	3.256 (3) Å × 2
	3.426 (2) Å × 3	3.431 (2) Å × 3	3.435(3) Å × 3	3.460 (2) Å × 3

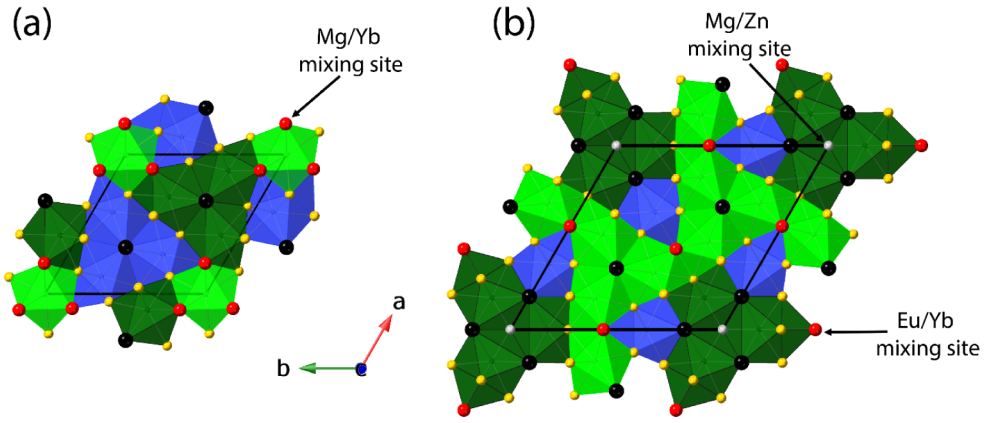

Figure 4. Structures of (a) $Eu_2Yb_{2.65}Mg_{9.35}Si_7$ ($Zr_2Fe_{12}P_7$-type) and (b) $Eu_{6.50}Yb_{1.50}Mg_{15.56}Zn_{0.44}Si_{12}$ ($Hf_2Co_4P_3$ type) viewed down the c-axis. Coordination of silicon sites are shown in polyhedral mode; the three unique silicon sites are shown as blue, light green, and dark green polyhedra. The mixed sites are highlighted for both structures. Mg sites are represented by yellow spheres, Yb/Mg or Yb/Eu sites by red spheres, Zn/Mg sites by gray spheres, and Eu sites are represented by black spheres.

latter forms as a line compound with a consistent composition, despite the possibility of Eu/Yb or Yb/Mg site mixing. It exhibits the $Zr_2Fe_{12}P_7$ structure type (Figure 4a) with europium occupying the two zirconium sites (1c and 1f Wyckoff sites) while ytterbium mixes with magnesium on one of the four iron sites (3k Wyckoff site). The three phosphorus sites are occupied by silicon. In this structure type, the 14 divalent cations are charge-balanced by 7 silicide anions. Changing the Eu/Yb ratio from 0.5/2.5 to 1.5/1.5 gives products with similar composition as confirmed by both SC-XRD refinement and EDS results (see Table S1 and S2, Supporting Information). This may indicate that having a 89% Yb and 11% Mg mixture on the 3k Wyckoff site (yielding the $Eu_2Yb_{2.65}Mg_{9.35}Si_7$ composition) is particularly stable.

Upon increasing the europium amount in the reaction, $Eu_5(Eu_xYb_{1-x})_3Mg_{16}Si_{12}$ analogs are formed. The switch from $Eu_2Yb_{2.65}Mg_{9.35}Si_7$ to $Eu_5(Eu/Yb)_3Mg_{16}Si_{12}$ is abrupt; they do not occur as mixed products. In $Eu_5(Eu/Yb)_3Mg_{16}Si_{12}$ analogs, the 2c and 3g sites are fully occupied by europium. These are the Ho sites in the $Ho_5Ni_{19}P_{12}$ structure; their full occupancy by europium reflects the relative sizes of the Eu^{2+} and Yb^{2+} cations (1.31 Å and 1.16 Å, respectively).[27] The 3f site exhibits Eu/Yb mixing, with occupancies shown in Table 3. The solid solution behavior is apparent, with the Eu content of this site increasing with the [Eu] in the reaction. This gradually increases the bond lengths around this 3f site, and with this, the unit cell parameters (from a = 14.6242 Å and c = 4.39690 Å for $Eu_{6.50}Yb_{1.50}Mg_{15.56}Zn_{0.44}Si_{12}$ to a = 14.7096 Å and c = 4.43040 Å for $Eu_8Mg_{15.71}Zn_{0.29}Si_{12}$).

Electronic Structure

The observation of a consistent composition $Eu_2Yb_{2.65}Mg_{9.35}Si_7$ instead of a solid solution that varies with Eu:Yb reactant ratio was unexpected. To better understand the preference for a line compound, Density of states (DOS) calculations were carried out on two model compounds, $Sr_2Mg_{12}Si_7$ and $Sr_2Ca_3Mg_9Si_7$ (Eu and Yb modeled as Sr and Ca, respectively). As seen in Figure 5, pseudogaps are seen at the Fermi level for both models, in agreement with their

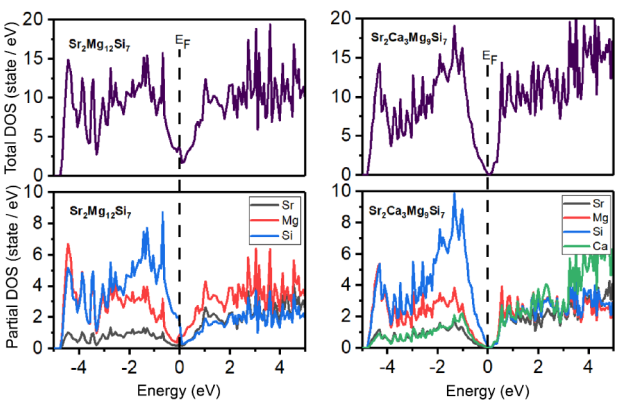

Figure 5. Total density of states data for $Sr_2Mg_{12}Si_7$ and $Sr_2Ca_3Mg_9Si_7$, model compounds for $Eu_2Yb_{2.65}Mg_{9.35}Si_7$. The E_F is set to 0 eV. The partial DOS contributions for Sr, Ca, Mg and Si elements are also shown.

https://doi.org/10.1021/acs.chemmater.5c02941
Chem. Mater. 2026, 38, 1875−1884

charge-balanced nature. Silicon states are dominant just below E_F. These compounds are therefore expected to be semimetals, with electrical conductivity occurring within the silicon lattice. The clearest difference between the models is that $Sr_2Ca_3Mg_9Si_7$ has a deeper gap at E_F than $Sr_2Mg_{12}Si_7$. This suggests that substitution of Yb onto the Mg site electronically stabilizes the compound, in agreement with the 90% occupancy of Yb consistently seen on this site.

Magnetic Behavior

Magnetic susceptibility data were collected on single crystals of $Eu_2Yb_{2.65}Mg_{9.35}Si_7$, $Eu_{6.50}Yb_{1.50}Mg_{15.56}Zn_{0.44}Si_{12}$, $Eu_{6.72}Yb_{1.28}Mg_{15.56}Zn_{0.44}Si_{12}$, $Eu_{7.46}Yb_{0.54}Mg_{15.56}Zn_{0.44}Si_{12}$ and $Eu_8Mg_{15.71}Zn_{0.29}Si_{12}$ to determine oxidation states and observe possible magnetic ordering. The oxidation states of the potentially magnetic elements (Eu and Yb) could be +2 or +3 or a mix of both. The presence of Eu/Yb or Yb/Mg mixed sites may induce complex magnetic behavior, as is seen for other disordered intermetallics.[28,29] Temperature-dependent magnetic susceptibility $\chi(T)$ for all compounds were measured with the magnetic field of 500 Oe applied parallel and perpendicular to the crystallographic c-axis and are shown in Figure 6. The data were fitted using the Curie–Weiss law $1/\chi_m = (T/C) - (\theta/C)$ at high temperature (in the paramagnetic state, 100 K $\leq T \leq$ 300 K) and the resulting parameters are shown in Table 4.

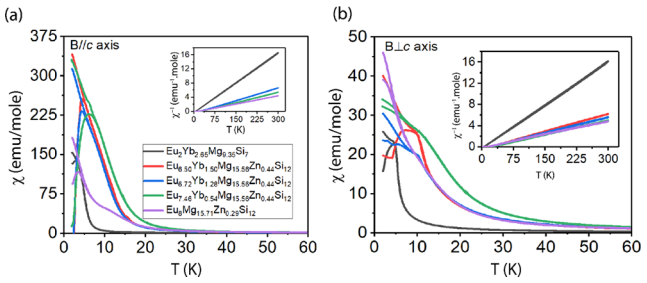

Figure 6. Magnetic susceptibility data for $Eu_2Yb_{2.65}Mg_{9.35}Si_7$, $Eu_{6.50}Yb_{1.50}Mg_{15.56}Zn_{0.44}Si_{12}$, $Eu_{6.72}Yb_{1.28}Mg_{15.56}Zn_{0.44}Si_{12}$, $Eu_{7.46}Yb_{0.54}Mg_{15.56}Zn_{0.44}Si_{12}$ and $Eu_8Mg_{15.71}Zn_{0.29}Si_{12}$ for both parallel (right) and perpendicular (left) orientations of the c-axis to the applied field of B = 500 Oe.

Magnetic susceptibility analysis along the two principal crystallographic directions reveals pronounced anisotropy in the Eu–Yb–Mg–Si series; the susceptibility values with the field applied parallel to the c-axis of the compounds are an order of magnitude larger than when applied perpendicular. The effective magnetic moments (μ_{eff}) per europium range between 7.18 and 8.62 μ_B, values generally consistent with the theoretical Eu^{2+} moment (7.94 μ_B). The Weiss temperatures (θ) range from 3.40 to 25.68 K, the positive values indicating predominantly ferromagnetic interactions. The data for all the compounds exhibit cusps and field-cooled/zero-field cooled splitting at temperatures below 15 K, indicating magnetic ordering phenomena. The T_C for the $Eu_5(Eu/Yb)_3Mg_{16}Si_{12}$ series does shift to slightly higher temperatures as the amount of europium is increased. A distinctly lower T_C is seen for $Eu_2Yb_{2.65}Mg_{9.35}Si_7$. The magnetic behavior of the endmember $Eu_8Mg_{15.71}Zn_{0.29}Si_{12}$ is somewhat different than that reported by Numakura in 2018.[24] Their report indicated antiferromagnetic ordering below T_N = 9.6 K and their magnetization data showed a slight metamagnetic transition that does not appear in the one measured here (vide infra). These differences may

Table 4. Magnetic Behavior (Observed Ordering and Magnetization Behavior, and Parameters Derived from Curie–Weiss Law) of Single Crystals Oriented with C-Axis Aligned Either Parallel or Perpendicular to B = 500 Oe Applied Field

Composition	T_C (K) (B//c)	T_C (K) (B⊥c)	μ (μ_B/Eu) (B//c)	μ (μ_B/Eu) (B⊥c)	θ (K) (B//c)	θ (K) (B⊥c)	H_C (Oe) (B//c)	H_C (Oe) (B⊥c)
$Eu_2Yb_{2.65}Mg_{9.35}Si_7$	5.9	5.29	8.45	8.62	5.58	3.96	50	190
$Eu_{6.50}Yb_{1.50}Mg_{15.56}Zn_{0.44}Si_{12}$	11.9	10.0	7.35	7.45	21.51	18.54	640	960
$Eu_{6.72}Yb_{1.28}Mg_{15.56}Zn_{0.44}Si_{12}$	11.5	10.0	7.18	7.77	22.05	14.73	590	500
$Eu_{7.46}Yb_{0.54}Mg_{15.56}Zn_{0.44}Si_{12}$	14.4	12.9	7.37	7.71	25.68	21.69	530	80
$Eu_8Mg_{15.71}Zn_{0.29}Si_{12}$	14.4	13.4	8.05	7.82	14.09	3.40	470	10

https://doi.org/10.1021/acs.chemmater.5c02941
Chem. Mater. 2026, 38, 1875–1884

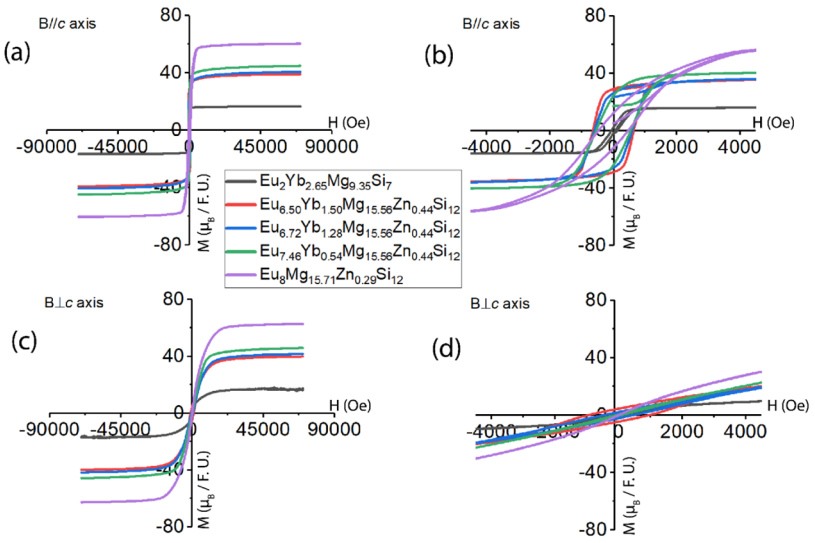

Figure 7. Field-dependent magnetization data for Eu−Yb−Mg−Si compounds with applied field parallel to the *c*-axis ((a) and (b), *top*) and perpendicular to the *c*-axis ((c) and (d), *bottom*). Data collected at 1.8 K.

be due to different synthetic methods and possible Zn doping on a Mg site in the compound studied here. The Mg/Zn mixed site is directly adjacent to the Eu1 site (see Figure 4b). Disorder on this site may serve to change the orientation of the magnetic moment and/or the nature of coupling to adjacent europium moments. Similar effects of disorder on nonmagnetic sites have been reported in systems such as $Er_2Cu_{0.92}Si_{2.76}$ and $Sm_3Ru_4Sn_{13-x}Ge_x$.[30,31]

The field-dependent magnetization data in the two different orientations (Figure 7) highlights the anisotropic behavior of these Eu−Yb−Mg−Si compounds. Magnetic saturation is reached at lower field for samples oriented with B//*c*-axis (5000 Oe) compared to when the same compounds are oriented with the field perpendicular to the *c*-axis (over 10000 Oe), indicating the *c*-axis is the easy axis. The saturation values scale with the amount of Eu in the compounds as expected. The Eu-rich end member, $Eu_8Mg_{15.71}Zn_{0.29}Si_{12}$, reaches ∼60 μ_B per formula unit at 10 kOe, close to the theoretical saturation moment expected for eight Eu^{2+} ions (7.94 μ_B/Eu^{2+}). Closer inspection at low field behavior (Figure 7, right) shows hysteresis is occurring, in agreement with the FC/ZFC splitting observed in Figure 6. The finite coercive fields and remanent magnetization are characteristic of ferromagnetic ordering. The coercive field H_C is larger for more Yb-rich analogs in the $Eu_5(Eu/Yb)_3Mg_{16}Si_{12}$ series, which may indicate Yb/Eu mixing on the 3f site serves to hinder domain wall motion.

Thermoelectric Properties

The temperature-dependent electrical resistivity (ρ) data for $Eu_2Yb_{2.65}Mg_{9.35}Si_7$, $Eu_{6.50}Yb_{1.50}Mg_{15.71}Zn_{0.44}Si_{12}$, $Eu_{6.72}Yb_{1.28}Mg_{15.71}Zn_{0.44}Si_{12}$, and $Eu_8Mg_{15.71}Zn_{0.29}Si_{12}$ are shown in Figure 8. The $Zr_2Fe_{12}P_7$-type line compound $Eu_2Yb_{2.65}Mg_{9.35}Si_7$ shows the highest resistivity across the full temperature range, starting above 5 mΩ·cm at low temperatures and gradually decreasing to around 2 mΩ·cm at 400 K. Compared to isostructural $Ba_{1.9}Ca_{2.4}Mg_{9.7}Si_7$ (0.5 to 0.8 mΩ·cm) at the same temperature range, $Eu_2Yb_{2.65}Mg_{9.35}Si_7$ is an order of magnitude higher.[17] The negative slope is characteristic of semiconducting-like behavior, indicating thermally activated carrier transport. This agrees with the density of

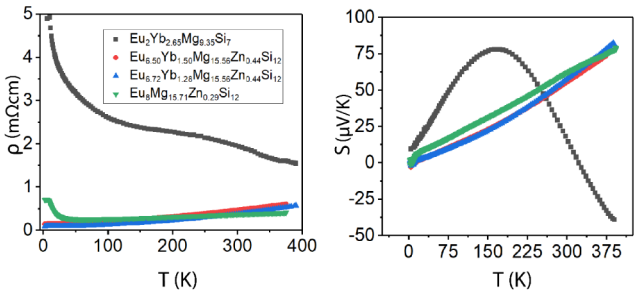

Figure 8. Temperature dependent electrical resistivity ρ (left), and Seebeck coefficient S (right), for $Eu_2Yb_{2.65}Mg_{9.35}Si_7$, $Eu_{6.50}Yb_{1.50}Mg_{15.71}Zn_{0.44}Si_{12}$, $Eu_{6.72}Yb_{1.28}Mg_{15.71}Zn_{0.44}Si_{12}$, and $Eu_8Mg_{15.71}Zn_{0.29}Si_{12}$.

states calculation showing a deep pseudogap at E_F (Figure 5), which leads to the semiconducting behavior of this analogue.

In contrast, the $Ho_5Ni_{19}P_{12}$-type series of compounds exhibit much lower resistivities, typically below 0.7 mΩ·cm, with a weakly positive temperature dependence at higher temperatures. Very similar behavior was seen for isostructural $Sr_{7.85}Mg_{16.15}Si_{12}$.[4] This metallic or degenerate semiconducting behavior suggests that their transport is dominated by carrier scattering rather than carrier activation. $Eu_{6.50}Yb_{1.50}Mg_{15.71}Zn_{0.44}Si_{12}$ and $Eu_{6.72}Yb_{1.28}Mg_{15.71}Zn_{0.44}Si_{12}$ show very similar ρ−T curves, while $Eu_8Mg_{15.71}Zn_{0.29}Si_{12}$ displays a slightly higher resistivity at low temperatures but converges with the others by ∼400 K. The low temperature cusp in the resistivity for $Eu_8Mg_{15.71}Zn_{0.29}Si_{12}$ corresponds to scattering of carriers as the magnetic ordering transition occurs; similar behavior was observed by Nukamura in their study of this compound.[24] The similarity in the resistivity behavior for the three $Eu_5(Eu_xYb_{1-x})_3Mg_{16}Si_{12}$ compounds suggests that electronic transport is occurring in silicon states and is not affected by the variation in cation mixing, which is in line with the desired "Phonon Glass-Electron Crystal" behavior for thermoelectric materials.[32,33]

The temperature dependences of the Seebeck coefficient (S) for $Eu_2Yb_{2.65}Mg_{9.35}Si_7$, $Eu_{6.50}Yb_{1.50}Mg_{15.71}Zn_{0.44}Si_{12}$, $Eu_{6.72}Yb_{1.28}Mg_{15.71}Zn_{0.44}Si_{12}$, and $Eu_8Mg_{15.71}Zn_{0.29}Si_{12}$ are shown in Figure 8. $Eu_2Yb_{2.65}Mg_{9.35}Si_7$ displays a pronounced

https://doi.org/10.1021/acs.chemmater.5c02941
Chem. Mater. 2026, 38, 1875−1884

maximum of ~85 μV/K at ~200 K, followed by a rapid decrease and eventual sign reversal above ~350 K, indicating a transition from p-type to n-type conduction. This non-monotonic behavior is characteristic of bipolar conduction, where thermally activated minority carriers reduce the net thermopower at high temperatures. In contrast, the $Eu_5(Eu/Yb)_3Mg_{16}Si_{12}$ compounds exhibit increases in S with temperature, remaining positive across the entire measured range suggesting stable p-type conduction.

The electronic thermal conductivity depends on the resistivity, calculated from ρ using Wiedemann–Franz law ($\kappa/\sigma = LT$), with the metallic $Eu_{6.50}Yb_{1.50}Mg_{15.71}Zn_{0.44}Si_{12}$, $Eu_{6.72}Yb_{1.28}Mg_{15.71}Zn_{0.44}Si_{12}$, and $Eu_8Mg_{15.71}Zn_{0.29}Si_{12}$ showing high κ_E and the semiconducting $Eu_2Yb_{2.65}Mg_{9.35}Si_7$ having a much lower value (Figure 9). The lattice thermal conductivity

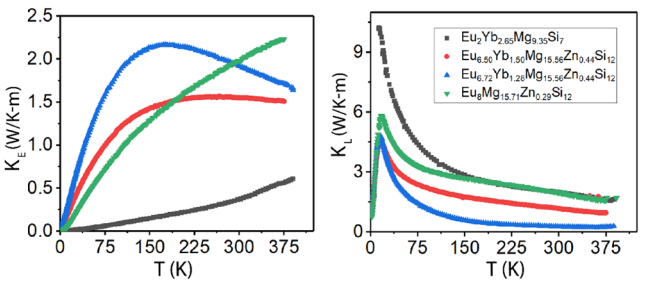

Figure 9. Temperature dependent electronic thermal conductivity (K_E) (left), and (right) lattice thermal conductivity (K_L) for $Eu_2Yb_{2.65}Mg_{9.35}Si_7$, $Eu_{6.50}Yb_{1.50}Mg_{15.71}Zn_{0.44}Si_{12}$, $Eu_{6.72}Yb_{1.28}Mg_{15.71}Zn_{0.44}Si_{12}$, and $Eu_8Mg_{15.71}Zn_{0.29}Si_{12}$.

clearly shows the impact of increasing disorder. The semiconducting $Eu_2Yb_{2.65}Mg_{9.35}Si_7$ and endmember $Eu_8Mg_{15.71}Zn_{0.29}Si_{12}$ have the highest κ_L. This is attributed to the smaller unit cell of $Eu_2Yb_{2.65}Mg_{9.35}Si_7$ and the lack of large cation (Yb) site mixing within the structure of $Eu_8Mg_{15.71}Zn_{0.29}Si_{12}$. The more complex structure and Eu/Yb mixed sites in $Eu_{6.50}Yb_{1.50}Mg_{15.71}Zn_{0.44}Si_{12}$ and $Eu_{6.72}Yb_{1.28}Mg_{15.71}Zn_{0.44}Si_{12}$ lead to lower κ_L. Mixing of zinc on the 1a magnesium site may also lower the thermal conductivity, but mixing on this site is consistent across the $Eu_5(Eu/Yb)_3Mg_{16}Si_{12}$ series.

Figure 10 illustrates the dimensionless figure of merit, zT, calculated from the S, ρ, and κ data for all four samples. The highest zT value is observed for $Eu_{6.72}Yb_{1.28}Mg_{15.71}Zn_{0.44}Si_{12}$, with a value of 0.14 at 400 K. This is slightly higher than the values seen for isostructural $Ba_{3.68}Sr_{4.07}Mg_{16.24}Si_{12}$ and $Sr_{7.85}Mg_{16.15}Si_{12}$ (zT = 0.08 and 0.11, respectively).[4] The

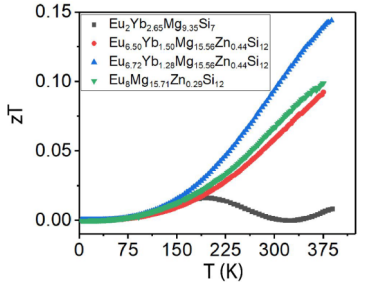

Figure 10. Dimensionless figure of merit zT as a function of the temperature for $Eu_2Yb_{2.65}Mg_{9.35}Si_7$, $Eu_{6.50}Yb_{1.50}Mg_{15.71}Zn_{0.44}Si_{12}$, $Eu_{6.72}Yb_{1.28}Mg_{15.71}Zn_{0.44}Si_{12}$, and $Eu_8Mg_{15.71}Zn_{0.29}Si_{12}$.

complex structure, incorporation of heavy elements, and Eu/Yb site mixing in $Eu_{6.72}Yb_{1.28}Mg_{15.71}Zn_{0.44}Si_{12}$ leads to the best balance of enhanced phonon scattering and electrical conductivity. The zT values for the $Eu_5(Eu/Yb)_3Mg_{16}Si_{12}$ series are below the desirable range (zT > 1); however, it is notable that the values are trending up with temperature (Figure 10) and likely to approach or exceed 1 at higher temperatures. This will be investigated in future experiments.

CONCLUSION

Reactions of silicon with a mixture of europium and ytterbium in magnesium-based flux have yielded large crystals of Zintl phases with two complex hexagonal structure types. While both structure types exhibit cation mixing on one site, it is notable that the $Zr_2Fe_{12}P_7$ type product $Eu_2Yb_{2.65}Mg_{9.35}Si_7$ appears to be a line compound due to electronic stabilization. This compound is also a semiconductor. In contrast, the $Hf_2Co_4P_3$-type $Eu_5(Eu/Yb)_3Mg_{16}Si_{12}$ materials show solid solution behavior and are metallic. The $Eu_{6.72}Yb_{1.28}Mg_{15.71}Zn_{0.44}Si_{12}$ analog exhibits the most promising thermoelectric behavior and measurements at high temperature are in progress. This work further demonstrates the flexibility of this structure type to incorporate divalent cations A = Ca, Sr, Ba, Eu, and Yb and the ability to tailor site mixing of these ions. Further work on $(A/A')_{5+x}Mg_{19-x}Si_{12}$ analogs will explore additional substitutions on the cation sites as well as on the silicon sites to optimize thermoelectric properties. Exploration of the Zn incorporation is also in progress; preliminary reactions using pure Mg as a flux are hindered by its higher melting point and viscosity compared to Mg/Zn or Mg/Al mixed fluxes.

ASSOCIATED CONTENT

Supporting Information

The Supporting Information is available free of charge at https://pubs.acs.org/doi/10.1021/acs.chemmater.5c02941.

Additional SEM-EDS data and mapping, tables of occupancies and bond lengths, and crystallographic tables (PDF)

Accession Codes

Deposition Numbers 2498651, 2498703–2498706, and 2498789 contain the supplementary crystallographic data for this paper. These data can be obtained free of charge via the joint Cambridge Crystallographic Data Centre (CCDC) and Fachinformationszentrum Karlsruhe Access Structures service.

AUTHOR INFORMATION

Corresponding Author

Susan E. Latturner – *Department of Chemistry and Biochemistry, Florida State University, Tallahassee, Florida 32306, United States;* orcid.org/0000-0002-6146-5333; Email: slatturner@fsu.edu

Authors

Olufemi S. Araoyinbo – *Department of Chemistry and Biochemistry, Florida State University, Tallahassee, Florida 32306, United States*

Amirhossein Zareihassangheshlaghi – *Department of Chemistry and Biochemistry, Florida State University, Tallahassee, Florida 32306, United States*

https://doi.org/10.1021/acs.chemmater.5c02941
Chem. Mater. 2026, 38, 1875–1884

Md Sahab Uddin − *Department of Chemistry and Biochemistry, Florida State University, Tallahassee, Florida 32306, United States*
Mehak Ghafoor − *National High Magnetic Field Laboratory, Tallahassee, Florida 32310, United States*
Kaya Wei − *National High Magnetic Field Laboratory, Tallahassee, Florida 32310, United States*

Complete contact information is available at: https://pubs.acs.org/10.1021/acs.chemmater.5c02941

Notes

The authors declare no competing financial interest.

■ ACKNOWLEDGMENTS

This work was funded by the National Science Foundation, Division of Materials Research (DMR-2126077). We gratefully acknowledge the FSU X-ray Characterization Center in the Department of Chemistry and Biochemistry at Florida State University, for access to essential facilities (FSU075000XRAY). Magnetic data were collected on a Quantum Design MPMS SQUID magnetometer acquired with NSF funding (MRI-2216125). Measurements of thermoelectric properties were carried out at the National High Magnetic Field Laboratory, which receives support from the National Science Foundation (DMR-2128556) and the State of Florida.

■ REFERENCES

(1) Kauzlarich, S. M. Zintl Phases: From Curiosities to Impactful Materials. *Chem. Mater.* **2023**, *35*, 7355−7362.
(2) Brown, S. R.; Kauzlarich, S. M.; Gascoin, F.; Snyder, G. J. $Yb_{14}MnSb_{11}$: New High Efficiency Thermoelectric Material for Power Generation. *Chem. Mater.* **2006**, *18*, 1873−1877.
(3) Zhang, W.; Chen, C.; Yao, H.; Xue, W.; Li, S.; Bai, F.; Huang, Y.; Li, X.; Lin, X.; Cao, F.; Sui, J.; Wang, S.; Yu, B.; Wang, Y.; Liu, X.; Zhang, Q. Promising Zintl-Phase Thermoelectric Compound SrAgSb. *Chem. Mater.* **2020**, *32*, 6983−6989.
(4) Zareihassangheshlaghi, A.; Galeano-Cabral, J.; Uddin, M. S.; Schundelmier, B.; Wei, K.; Baumbach, R. E.; Latturner, S. E. Synthesis of Zintl Phase Metal Silicide Thermoelectric Materials in Magnesium/Zinc Flux. *Inorg. Chem.* **2024**, *63*, 20186−20196.
(5) Ma, X.; Lu, J.; Whalen, J. B.; Latturner, S. E. Flux Growth and Magnetoresistance Behavior of Rare Earth Zintl phase EuMgSn. *Inorg. Chem.* **2013**, *52*, 3342−3348.
(6) Jiang, J.; Kauzlarich, S. M. Colossal Magnetoresistance in a Rare Earth Zintl Compound with a New Structure Type: $EuIn_2P_2$. *Chem. Mater.* **2006**, *18*, 435−441.
(7) Corbett, J. D.*In Solid State Chemistry: Techniques*Cheetham, A. K.; Day, P.Oxford University PressOxford, UK19871 pp. 1−35
(8) Kanatzidis, M. G.; Pöttgen, R.; Jeitschko, W. The Metal Flux: A Preparative Tool for the Exploration of Intermetallic Compounds. *Angew. Chem., Int. Ed.* **2005**, *44*, 6996−7023.
(9) Vasquez, G.; Huq, A.; Latturner, S. E. In Situ Neutron Diffraction Studies of the Metal Flux Growth of Ba/Yb/Mg/Si Intermetallics. *Inorg. Chem.* **2019**, *58*, 8111−8119.
(10) Uddin, M. S.; Zareihassangheshlaghi, A.; Latturner, S. E. Temperature-Dependent products in Gallium Flux Reactions of Cerium and Transition Metals. *Inorganic Chem.* **2024**, *63* (30), 13865−13874.
(11) Blake, N. P.; Bryan, D.; Latturner, S.; Møllnitz, L.; Stucky, G. D.; Metiu, H. Structure and stability of the clathrates $Ba_8Ga_{16}Ge_{30}$,$Sr_8Ga_{16}Ge_{30}$,$Ba_8Ga_{16}Si_{30}$, and $Ba_8In_{16}Sn_{30}$. *J. Chem. Phys.* **2001**, *114*, 10063−10074.
(12) Chen, X. Z.; Larson, P.; Sportouch, S.; Brazis, P.; Mahanti, S. D.; Kannewurf, C. R.; Kanatzidis, M. G. Molten Ga as a Solvent for Exploratory Synthesis. Preparation, Structure, and Properties of Two Ternary Silicides $MNiSi_3$ (M = Sm, Y). *Chem. Mater.* **1999**, *11*, 75−83.
(13) Jayasinghe, A.; Lai, Y.; Baumbach, R.; Latturner, S. E. $U_{1.33}T_4Al_8Si_2$ (T = Ni, Co): Complex Uranium Silicides Grown from Aluminum/Gallium Flux Mixtures. *Inorganic Chem.* **2019**, *58*, 12209−12217.
(14) Latturner, S. E.; Bilc, D.; Mahanti, S. D.; Kanatzidis, M. G. $RE_2MAl_6Si_4$ (RE= Gd, Tb, Dy; M= Au, Pt): Layered quaternary intermetallics featuring $CaAl_2Si_2$-type and $YNiAl_4Ge_2$-type slabs grown from aluminum flux. *Inorg. Chem.* **2003**, *42*, 7959−7966.
(15) Peter, S. C.; Kanatzidis, M. G. $ThSi_2$ Type Ytterbium Disilicide and its Analogues YbT_xSi_{2-x} (T = Cr, Fe, Co). *Z. Anorg. Allg. Chem.* **2012**, *638*, 287−293.
(16) Aguirre, R.; Eder, F.; von Rohr, F. O.; Thomas, A. A. New Phases in the Sc−Mn−Si and Sc−Mn−Al−Si Systems Through Molten Indium Flux Synthesis. *Helv. Chim. Acta* **2024**, *107* (4), No. e202400018.
(17) Silsby, K.; Sui, F.; Ma, X.; Kauzlarich, S. M.; Latturner, S. E. Thermoelectric Properties of $Ba_{1.9}Ca_{2.4}Mg_{9.7}Si_7$: A New Silicide Zintl Phase with the $Zr_2Fe_{12}P_7$ Structure Type. *Chem. Mater.* **2015**, *27*, 6708−6716.
(18) Vasquez, G.; Wei, K.; Choi, E. S.; Baumbach, R.; Latturner, S. E. Magnesium-Based Flux Growth and Structural Relationships of a Large Family of Tetrelide Semimetals. *Crystal Growth Design* **2020**, *20*, 2632−2643.
(19) Sheldrick, G. M. Crystal Structure Refinement with SHELXL. *Acta Cryst. C: structural Chem.* **2015**, *71*, 3−8.
(20) Toby, B. H.; Von Dreele, R. B. GSAS-II: The genesis of a modern open-source all-purpose crystallography software package. *J. Appl. Crystallogr.* **2013**, *46*, 544−549.
(21) Blochl, P. E.; Jepsen, O.; Andersen, O. K. Improved Tetrahedron Method for Brillouin-Zone Integrations. *Phys. Rev. B* **1994**, *49*, 16223−16233.
(22) Tank, R.; Jepsen, O.; Burkhardt, A.; Andersen, O. K. *The TB-LMTO- ASA Program*. Max-Planck-Institut f{\"u}r Festk{\"o}rperforschung: Stuttgart, Germany, 1994.
(23) Xie, Q.; Kubata, C.; Wörle, M.; Nesper, R. Tt-Tt (Tt = Si, Ge) Dumb-Bell Structures at Different Valence Electron Concentrations: Ln_2MgSi_2 (Ln = La, Ce), $Yb_2Li_{0.5}Ge_2$, and $Yb_{1.75}Mg_{0.75}Si_2$. *Z. Anorg. Allg. Chem.* **2008**, *634*, 2469−2476.
(24) Numakura, R.; Iizuka, R.; Michimura, S.; Katano, S.; Kosaka, M. Single Crystal Growth and Physical Properties of the new Ternary Compound $Eu_2Mg_4Si_3$. *Physica B: condensed Matter.* **2018**, *536*, 262−266.
(25) Perri, J. A.; Binder, I.; Post, B. Rare Earth Metal Disilicides. *J. Phys. Chem.* **1959**, *63*, 616−619.
(26) Pöttgen, R.; Hoffmann, R. D.; Kussmann, D. The binary silicides Eu_5Si_3 and Yb_3Si_5 − synthesis, crystal structure and chemical bonding. *Z. Anorg. Allg. Chem.* **1998**, *624*, 945−951.
(27) Shannon, R. D. Revised Effective Ionic Radii and Systematic Studies of Interatomic Distances in Halides and Chalcogenides. *Acta Crystallogr. A* **1976**, *32*, 751−767.
(28) Zaikina, J. V.; Schellenberg, I.; Benbow, E. M.; Pöttgen, R.; Latturner, S. E. Influence of the La/M Network on Magnetic Properties of Mn_4 Tetrahedra in Intermetallic Compounds $La_{21-\delta}Mn_8M_7C_{12}$ (M = Ge, Sn, Sb, Te, Bi). *Chem. Mater.* **2016**, *23*, 1768−1778.
(29) Kovnir, K.; Garlea, V. O.; Thompson, C. M.; Zhou, H. D.; Reiff, W. M.; Ozarowski, A.; Shatruk, M. Spin-Glass Behavior in $LaFe_xCo_{2-x}P_2$ Solid Solutions: Interplay Between Magnetic Properties and Crystal and Electronic Structures. *Inorg. Chem.* **2011**, *50*, 10274−10283.
(30) Gomes-Silva, M.; Dias dos Santos, R. J.; Franca, J. K. P.; Lang, R.; dos Santos, A. O.; da Silva, L. M. On the nonmagnetic atom disorder influence in the magnetic and magnetocaloric properties of the $Er_2Cu_{0.92}Si_{2.76}$ off-stoichiometric single-phase compound. *J. Alloys Cmpds* **2025**, *1010*, 177338.

(31) Fritsky, J. W.; Zhai, H. F.; Zhao, Y.; Rauniyar, A.; Botana, A. S.; Khoury, J. F. Preferential Site Ordering Alters the Magnetic Behavior of $Sm_3Ru_4Sn_{13-x}Ge_x$ (x = 0−2). *Inorg. Chem.* **2025**, *64*, 19679−19687.
(32) Slack, G. A.; Rowe, D. *CRC Handbook of Thermoelectrics*; CRC press: Boca Raton, FL, 1995.
(33) Kauzlarich, S. M.; Zevalkink, A.; Toberer, E.; Snyder, G. J. Zintl Phases: Recent Developments in Thermoelectrics and Future Outlook. *Thermoelectric Materials and Devices*. Nandhakumar, I.; White, N. M.; Beeby, S. pp. 1−26.The Royal Society of Chemistry, 2016

https://doi.org/10.1021/acs.chemmater.5c02941
Chem. Mater. 2026, 38, 1875−1884